

**THE EFFECT OF THERMAL BUOYANCY
IN THE MIXED CONVECTIVE FLOWS
THROUGH A VERTICAL CHANNEL
WITH A BUILT-IN
CIRCULAR CYLINDER**

A THESIS SUBMITTED
IN PARTIAL FULFILMENT OF THE REQUIREMENTS
FOR THE DEGREE OF
MASTER OF TECHNOLOGY

by
Suresh Singh



to the
DEPARTMENT OF MECHANICAL ENGINEERING
INDIAN INSTITUTE OF TECHNOLOGY
KANPUR-208016 INDIA
APRIL 1998

20 MAY 1998 / ME

CENTRAL LIBRARY

IIT KANPUR

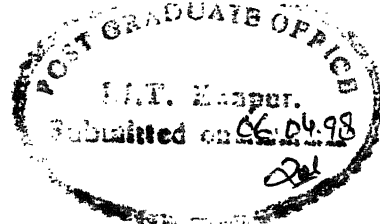
No. A12548

ME-1998-M-SIN-EFF

Entered in System
Nimisha
25.6.98



A125482



18855

CERTIFICATE

It is certified that the work contained in the thesis entitled "*The effect of thermal buoyancy in the mixed convective flows through a vertical channel with a built-in circular cylinder*", by *Mr. Suresh Singh*, has been carried out under my supervision and that this work has not been submitted elsewhere for a degree.

Gautam Biswas

Gautam Biswas

Professor

Department of Mechanical Engineering

I.I.T. Kanpur

April, 1998.

ACKNOWLEDGMENT

I express my sincere gratitude to Prof. G. Biswas for his academic guidance and moral support during the course of this study. It is indeed very difficult to find words to thank him for the kind of motivation and the urge for academic pursuits he instilled in me.

I am greatly obliged to other professors, the senior student fraternity and the staff associated with the CFD Lab. for their invaluable suggestions and help time and again.

The contribution of Mr. Veerabathraswamy K., my senior colleague, is gratefully acknowledged for providing the preliminary version of the code which was thoroughly modified during the course of present work.

It is a pleasure to remember all my friends with whom I shared an enjoyable and fruitful period of my life.

I shall always cherish the memories of my stay and the rememberances of all those who walked down the road of life with me at I.I.T Kanpur.

(Suresh Singh)

ABSTRACT

The flow field and the temperature distribution around a heated/cooled circular cylinder placed in an insulated vertical channel is determined using a novel finite volume algorithm which combines some important features of the finite element methods with the finite difference based techniques. Elementwise interpolation (iso-parametric) and transformation of non-orthogonal element geometry into a square computational element have been made use of while solving the integral conservation equations. Unsteady mixed convection situation has been considered for the study and the effect of buoyancy on the vortex shedding in the wake of a cylinder has been observed for a fixed Reynolds number of 100. Vortex shedding at $Re=100$ is found to stop completely at a critical Richardson number of 0.15. Below this critical value of Richardson number, shedding of vortices into the stream is quite prominent. Heat transfer characteristics of the heated/cooled cylinder are studied as a function of Richardson number. The results are of use in the design of shell and tube heat exchangers.

Contents

Certificate	i
Acknowledgment	ii
Abstract	iii
List of Figures	vi
Nomenclature	vii
1 INTRODUCTION	1
1.1 Flow past bluff bodies	1
1.2 Mixed Convection	2
1.3 Literature Review	3
2 STATEMENT OF THE PROBLEM	8
2.1 Domain Definition	8
2.2 Governing Equations	8
2.3 Boundary Conditions	13
3 METHOD OF SOLUTION	15
3.1 Description of the Extra-Flag algorithm	15
3.2 Upwinding of Convection Terms	25
3.3 Derivation of Pressure Correction Equation	26

4 RESULTS AND DISCUSSION	32
5 CONCLUSION	42
Bibliography	43

List of Figures

- Fig.1 Schematic representation of the domain
- Fig.2 Grid (a)Complete channel (b)Near the cylinder
- Fig.3 (a)Domain descritization (b)Interpolation domain for momentum balance
- Fig.4 Transformation of a curvilinear control volume
into a square computational cell
- Fig.5 Pressure-velocity coupling for a
continuity control volume
- Fig.6 Streamlines
- Fig.7 Isotherms
- Fig.8 Phase diagrams (U vs. V plots)
- Fig.9 Transverse velocity signal vs. Non-dimensional time
and FFT for $Ri=-1.0$ and $Ri=0$ cases
- Fig.10 Strouhal number vs. Richardson number
- Fig.11 Average Nusselt number vs. Richardson number
- Fig.12 Local Nusselt number variation over the cylinder surface
- Fig.13 Comparison of results($Re=40$,far field boundary condition)
(a) Local Nusselt number
(b) Strouhal number

Nomenclature

A	Area of the control volume
CV1	continuity control volume
CV2	momentum control volume
D	Diameter of the cylinder
f	Shedding frequency
Gr	Grashoff number $(g\beta(T_w - T_\infty)D^3)/\nu^2$
H	Channel width
k	thermal conductivity of the fluid
n_x, n_y	Direction cosines of outward unit normal on the control volume faces
\overline{Nu}_{av}	Time and space averaged Nusselt number
\overline{Nu}_ϕ	Time averaged local Nusselt number
p	pressure
P	Non-dimensional pressure $p/(\rho V_{av}^2)$
Pr	Prandtl number $(\mu c_p)/k$
Re	Reynolds number $(V_{av}D)/\nu$
Ri	Richardson number Gr/Re^2
St	Strouhal number $(fD)/V_{av}$
t	time
T	absolute temperature

- u transverse velocity
- U Non-dimensional transverse velocity u/V_{av}
- v streamwise velocity
- V Non-dimensional longitudinal velocity v/V_{av}
- x transverse direction of the coordinates
- X Non-dimensional length in x-direction x/D
- y streamwise direction of the coordinates
- Y Non-dimensional length in y-direction y/D

Greek Symbols

- α upwinding factor
- β thermal expansion coefficient of the fluid
- μ dynamic viscosity of the fluid
- ν kinematic viscosity of the fluid
- ρ density of the fluid
- ϕ Angle
- τ Non-dimensional time $(tV_{av})/D$
- θ Non-dimensional temperature $(T - T_\infty)/(T_w - T_\infty)$
- ξ, η Coordinates in the computational cell

Subscripts

av average

b upstream node

w wall

∞ condition at the channel inlet

Superscripts

n timelevel

$*$ provisional quantity

Chapter 1

INTRODUCTION

1.1 Flow past bluff bodies

The flow past bluff bodies has been a fascinating problem both for academic and industrial applications. The behaviour of the flow in the wake of a bluff body is responsible for changes in heat transfer and flow induced vibrations on the body. Flow separation and vortex shedding tend to increase the heat transfer but at the same time increase the drag on the body. The shedding may prove to be detrimental for the life of the body. The objective of getting maximum heat transfer without being affected much by the flow induced vibrations provides with enough challenge in this field of study.

Understanding of the flow past a bluff body is useful for the design of heat exchangers, air conditioning coils, nuclear reactor fuel rods, chimney stacks, T.V towers, suspension bridges etc. The Reynolds number associated with these flows are sufficiently high to produce turbulent flows in the wake region even if

the boundary layer remains laminar. Slaouti and Gerrard(1992) have pointed out that there is no general turbulence model to incorporate into the numerical simulation of unsteady separated flows. Direct numerical simulation of Navier-Stokes equations is possible but it requires large computing power. It has been observed in experiments that some features of large scale wake behaviour associated with vortex shedding at high Reynolds number are similar to that at low Reynolds numbers. At low Reynolds numbers, predicting flows and heat transfer around a cylinder may be reasonably good by two-dimensional laminar computations.

1.2 Mixed Convection

The difference in temperature of the bluff body and the fluid in many practical situations demand the study of mixed convection. In a vertical flow, the velocity induced by free convection will be either aligned or opposed to that of the forced convection. It has been observed that in the presence of aligned free and forced convection, the wake region is diminished and the separation points are shifted downstream. When the free convection acts in the opposite direction the point of separation is advanced upstream.

1.3 Literature Review

Fromm and Harlow [1], Thoman and Szewczyk [2] and Jain and Goel [3] have studied numerically flow past a circular cylinder. Forced convection over a row of inline cylinders placed between parallel plates has been studied by Kundu *et al* [4, 5]. The effect of buoyancy on the flow structure has not been taken into consideration in the above investigations. When flow velocity is not very high and the temperature difference between the bluff body and the fluid is significantly high, the heat transfer characteristics are strongly influenced by thermal buoyancy effects. In many practical applications, the cylinder is placed inside a confined space so that the side walls have considerable influence on the heat transfer rate. Quite a few efforts dealing with mixed convection regime have used steady state equations and are limited to small Reynolds numbers up to 40 (Farouk and Guceri [6] and Badr [7]).

Biswas *et al* [8] have studied unsteady mixed convection heat transfer in a horizontal channel with a built-in square cylinder. They have found that for a given Reynolds number, the heating of the fluid in the channel is improved by mixed convection up to a certain Grashoff number and deteriorates if the Grashoff number is further increased. Oosthuizen and Madan [9] studied experimentally mixed convection for Reynolds number ranging between 100 and 300. Noto and Matsumoto [10, 12] reported degeneration of unsteady vortices

to the stationary ones and termed it as the *breakdown of von-Karman street*. Chang and Sa [13] have studied the behaviour of the near wake vortices. They have predicted the degeneration of purely periodic flows into a steady vortex pattern at a critical Grashoff number of 1500.

The present study considers an unsteady mixed convection flow over a circular cylinder placed inside an insulated vertical channel. In order to compare the results of present investigation with that of Badr [7] and Dennis *et al* [19], some computations have been performed for the situation concerning flow over a heated cylinder placed in an infinite medium. Extra-Flag algorithm proposed by Mukhopadhyay *et al* [14] has been used for the analysis.

Chapter 2

STATEMENT OF THE PROBLEM

2.1 Domain Definition

The system of interest consists of a vertical channel with insulated side walls.

An obstacle in the form of a circular cylinder is placed inside it (Fig.1). The blockage ratio (D/H) is equal to 0.25 and the length of the channel is twenty four times the diameter (D) of the cylinder. The centre of the cylinder is placed on the vertical axis of the channel at a downstream distance of $8D$ from the entry plane .

2.2 Governing Equations

The domain is discretized into small curvilinear quadrilateral cells (Figs.2,3).

The velocity and temperature nodes are located at the vertices, and the pressure nodes are located at the centroids of these cells. The continuity control

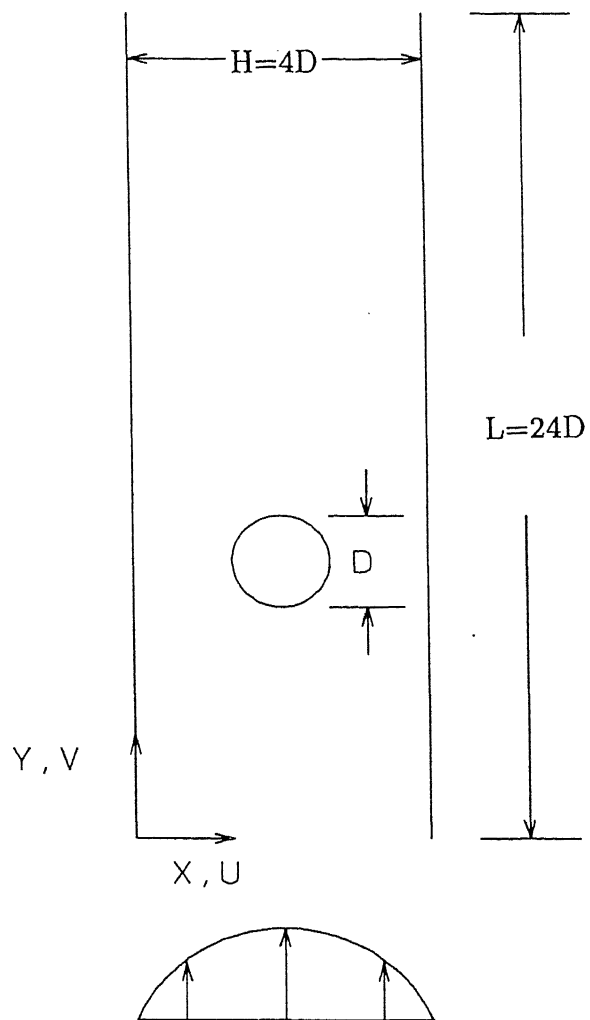
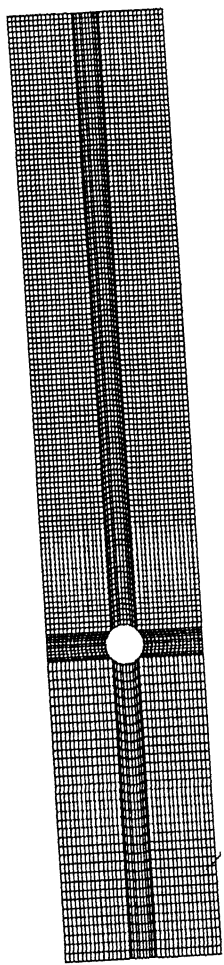
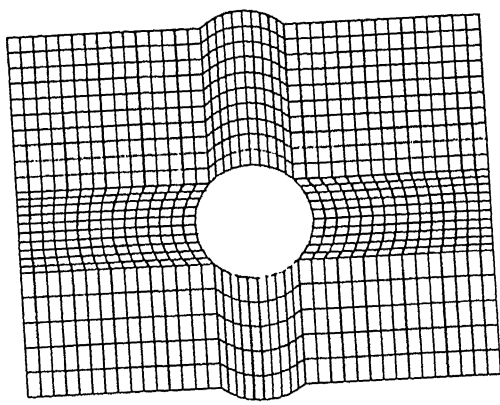


Fig.1 Schematic representation of the domain

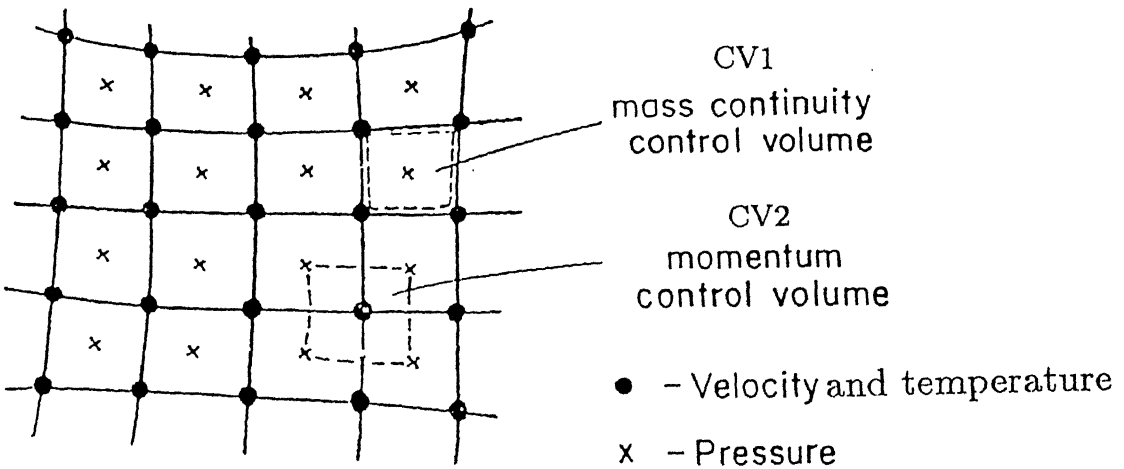


(a) Complete channel

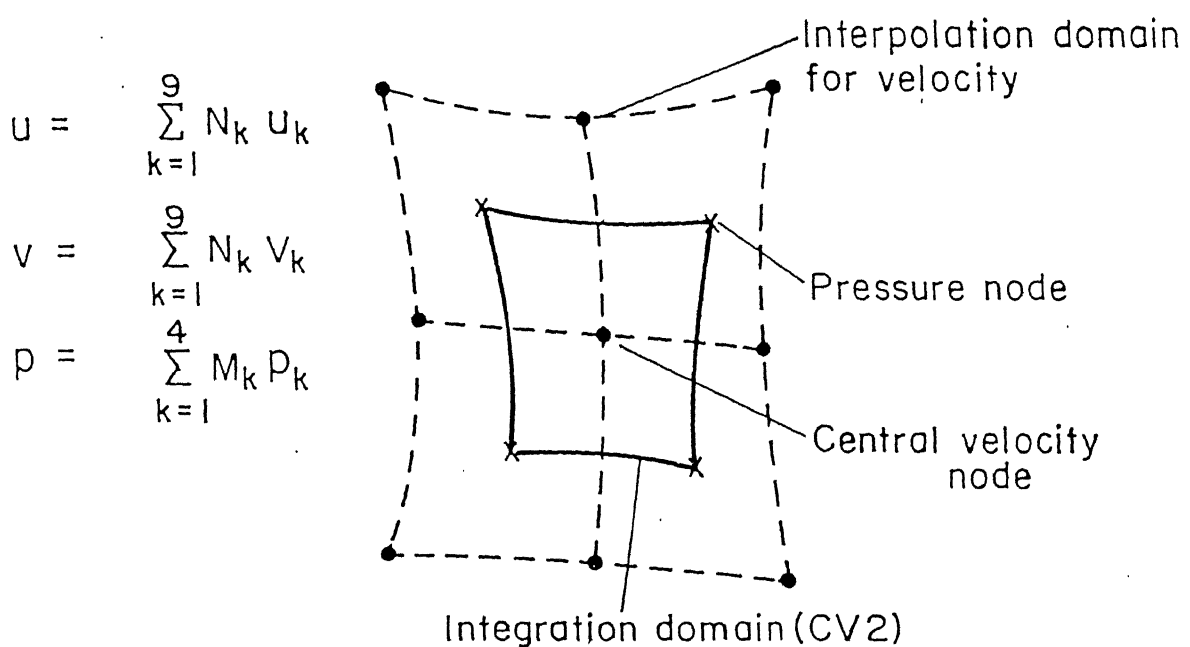


(b) Near the cylinder

Fig.2 Grid



(a) Schematic representation of the discretization



(b) Interpolation domain for momentum balance

Fig.3 Domain discretization

volumes (**CV1**) are formed by the grid lines connecting velocity nodes and the momentum control volumes (**CV2**) are formed by curvilinear quadrilaterals whose vertices are the pressure nodes .

Considering a typical control volume for mass continuity, **CV1**, the integral form of the mass balance can be written as

$$\frac{\partial}{\partial t} \iint_{cv1} \rho dA + \int_{cs1} \rho \underline{V} \cdot \hat{n} dl = 0 \quad (2.1)$$

where, dl is an elemental length on the boundary **CS1** of the control volume **CV1**, and \hat{n} is the local outward normal vector. For incompressible flow, the first term of the equation(2.1) is identically zero, which simplifies the equation to

$$\int_{cs1} \underline{V} \cdot \hat{n} dl = \int_{cs1} (u n_x + v n_y) dl = 0 \quad (2.2)$$

where, n_x and n_y are the direction cosines of the outward normal \hat{n} on the boundary **CS1**.

Now considering any typical momentum control volume **CV2**, the integral form of x and y momentum balance equations can be written as

$$\frac{\partial}{\partial t} \iint_{cv2} u (\rho dA) + \int_{cs2} u (\rho \underline{V} \cdot \hat{n} dl) = F_x \quad (2.3)$$

$$\frac{\partial}{\partial t} \iint_{cv2} v (\rho dA) + \int_{cs2} v (\rho \underline{V} \cdot \hat{n} dl) = F_y \quad (2.4)$$

where F_x and F_y are the components of the resultant forces acting on the

control volume in x and y directions respectively. These can be evaluated as

$$\begin{aligned} F_x &= \hat{i} \cdot \int_{cs2} \underline{\sigma} \cdot \hat{n} dl \\ &= \hat{i} \cdot \int_{cs2} \left\{ -p \underline{I} + \mu (\nabla \underline{V} + \nabla \underline{V}^T) - \frac{2}{3} \mu (\nabla \cdot V) \underline{I} \right\} \cdot \hat{n} dl \end{aligned} \quad (2.5)$$

where $\underline{\sigma}$ is the stress. For incompressible flows

$$F_x = \int_{cs2} \left\{ -pn_x + 2\mu \frac{\partial u}{\partial x} n_x + \mu \left(\frac{\partial u}{\partial y} + \frac{\partial v}{\partial x} \right) n_y \right\} dl \quad (2.6)$$

For the y momentum equation,

$$F_y = \hat{j} \cdot \int_{cs2} \underline{\sigma} \cdot \hat{n} dl + \hat{j} \cdot \iint_{cv2} \rho g \beta (T - T_\infty) dA \quad (2.7)$$

where T is the absolute temperature. The second term in the above equation is due to buoyancy force. For incompressible flows

$$\begin{aligned} F_y &= \int_{cs2} \left\{ -pn_y + 2\mu \frac{\partial u}{\partial y} n_y + \mu \left(\frac{\partial u}{\partial y} + \frac{\partial v}{\partial x} \right) n_x \right\} dl \\ &\quad + \iint_{cv2} \rho g \beta (T - T_\infty) dA \end{aligned} \quad (2.8)$$

Finally the x and y momentum equations can be written as

$$\begin{aligned} \rho \left\{ \frac{\partial}{\partial t} \iint_{cv2} u dA + \int_{cs2} u(un_x + vn_y) dl \right\} &= \\ \int_{cs2} \left\{ -pn_x + 2\mu \frac{\partial u}{\partial x} n_x + \mu \left(\frac{\partial u}{\partial y} + \frac{\partial v}{\partial x} \right) n_y \right\} dl \end{aligned} \quad (2.9)$$

$$\begin{aligned} \rho \left\{ \frac{\partial}{\partial t} \iint_{cv2} v dA + \int_{cs2} v(un_x + vn_y) dl \right\} = \\ \int_{cs2} \left\{ -pn_y + 2\mu \frac{\partial v}{\partial y} n_y + \mu \left(\frac{\partial u}{\partial y} + \frac{\partial v}{\partial x} \right) n_x \right\} dl \\ + \iint_{cv2} \rho g \beta (T - T_\infty) dA \end{aligned} \quad (2.10)$$

Now considering a typical control volume, CV2, the integral form of the energy equation can be written as

$$\frac{\partial}{\partial t} \iint_{cv2} e(\rho dA) + \int_{cs2} (\underline{V}e) \cdot \hat{n} dl = \int_{cs2} k \nabla T \cdot \hat{n} dl + \iint_{cv2} Q dS \quad (2.11)$$

where e is the internal energy, k is the thermal conductivity, T is the temperature of the fluid, and Q is the volumetric rate of heat generation. For the case with no heat source, Q is identically equal to zero. For incompressible flows,

$$cT = e$$

where c is the specific heat and it is a constant (which is a reasonable assumption for incompressible flows). With this substitution, the energy equation becomes

$$\rho \left\{ \iint_{cv2} T dS + \int_{cs2} T(un_x + vn_y) dl \right\} = \int_{cs2} \frac{k}{c} \left\{ \frac{\partial T}{\partial x} n_x + \frac{\partial T}{\partial y} n_y \right\} dl \quad (2.12)$$

The non-dimensionalized form of the equations is as follows:

$$\int_{cs1} (U n_x + V n_y) dl = 0 \quad (2.13)$$

$$\left\{ \frac{\partial}{\partial \tau} \iint_{cv2} U dA + \int_{cs2} U (U n_x + V n_y) dl \right\} =$$

$$\int_{cs2} \left\{ -P n_x + \frac{2}{Re} \frac{\partial U}{\partial X} n_x + \frac{1}{Re} \left(\frac{\partial U}{\partial Y} + \frac{\partial V}{\partial X} \right) n_y \right\} dl \quad (2.14)$$

$$\left\{ \frac{\partial}{\partial \tau} \iint_{cv2} V dA + \int_{cs2} V (U n_x + V n_y) dl \right\} =$$

$$\begin{aligned} \int_{cs2} \left\{ -P n_y + \frac{2}{Re} \frac{\partial V}{\partial Y} n_y + \frac{1}{Re} \left(\frac{\partial U}{\partial Y} + \frac{\partial V}{\partial X} \right) n_x \right\} dl \\ + \frac{Gr}{Re^2} \iint_{cv2} \theta dA \end{aligned} \quad (2.15)$$

$$\begin{aligned} \left\{ \frac{\partial}{\partial \tau} \iint_{cv2} \theta dA + \int_{cs2} \theta (U n_x + V n_y) dl \right\} = \\ \int_{cs2} \left\{ \frac{1}{Pr Re} \left(\frac{\partial \theta}{\partial X} n_x + \frac{\partial \theta}{\partial Y} n_y \right) dl \right\} \end{aligned} \quad (2.16)$$

2.3 Boundary Conditions

Parabolic velocity profile at ambient temperature is assumed at the inlet. The channel walls are insulated. The cylinder temperature is governed by the magnitude of the Richardson number. No-slip boundary condition is imposed both on the cylinder and the channel walls. The exit boundary is located at far downstream so that it does not influence the vortices in the near wake region. However, at the outlet, the derivative of the variables is made equal to zero.

Mathematically one can write

at the inlet

$$U = \theta = 0 ; V = V(X)$$

at the outlet

$$\frac{\partial U}{\partial Y} = 0 ; \frac{\partial V}{\partial Y} = 0 ; \frac{\partial \theta}{\partial Y} = 0$$

at the channel walls

$$U = V = \frac{\partial \theta}{\partial X} = 0$$

at the cylinder surface

$$U = V = 0 ; \theta = 1$$

Some cases have been computed to simulate the flow past a circular cylinder placed in an infinite medium. For such a simulation, the blockage ratio (D/H) has been taken as 0.1. The boundary conditions at the side walls have been modified to simulate the far field boundary. The boundary conditions for the infinite medium situation are as follows :

at the inlet

$$U = \theta = 0 ; V = 1.0$$

at the outlet

$$\frac{\partial U}{\partial Y} = 0 ; \frac{\partial V}{\partial Y} = 0 ; \frac{\partial \theta}{\partial Y} = 0$$

on the sides

$$U = \theta = 0 ; V = 1.0$$

at the cylinder surface

$$U = V = 0 ; \theta = 1$$

Chapter 3

METHOD OF SOLUTION

3.1 Description of the Extra-Flag algorithm

The EXTRA-FLAG algorithm proposed by Mukhopadhyay *et al* [14] has been extended for the present work. The energy equation is solved together with the Navier-Stokes equation. EXTRA-FLAG algorithm is based on integral mass, momentum and energy balance applied over the non-orthogonal control volume. The integral flow equations are converted into algebraic form through numerical quadrature coupled with spatial interpolation (isoparametric) of their nodal values. In order to facilitate the numerical quadrature, each non-orthogonal quadrilateral control volume is mapped into a standard square cell with the help of the local curvilinear coordinates. Explicit time marching is employed for the momentum equations using the pressure field corresponding to the previous time level. Principle of elemental mass conservation, on the other hand, is enforced in an implicit manner by iteratively correcting the

velocity and pressure fields. The method of solution thus utilises the geometrically additive features of FEM (isoparametric interpolation and numerical quadrature) with the control volume approach applied in MAC [15] and SIMPLE [16] family of algorithms.

Since the order of the momentum equations is one order higher than the continuity equation, the velocities have been interpolated using bi-quadratic functions, while applying the momentum principle. For the satisfaction of continuity, bilinear interpolation functions have been used to describe the velocity variables over the respective control volumes. The temperature interpolation is similar to that of the velocities for the momentum control volume. It can be represented mathematically as follows :

For continuity equation

$$U = \sum_{k=1}^4 M_k U_k ; V = \sum_{k=1}^4 M_k V_k \quad (3.1)$$

For momentum and energy equation

$$U = \sum_{k=1}^9 N_k U_k ; V = \sum_{k=1}^9 N_k V_k ; \theta = \sum_{k=1}^9 N_k \theta_k \quad (3.2)$$

The summation in equation (3.1) is performed by making use of velocities at the four vertices of the continuity control volume. Equation (3.2) uses the velocities of the neighbouring nodes of the corresponding momentum control

volume. These are shown in Fig.3. The variation of the pressure over the momentum control volume is expressed in the form

$$P = \sum_{k=1}^4 M_k P_k \quad (3.3)$$

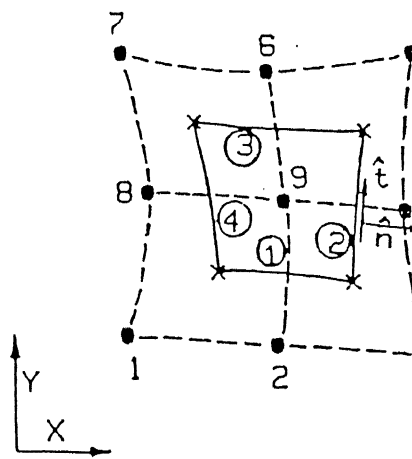
In the equations , M_k and N_k are the interpolation functions, and are given by

$$\begin{aligned} N_1 &= \frac{1}{64}\xi\eta(\eta-2)(\xi-2) ; & N_2 &= \frac{1}{32}\eta(4-\xi^2)(\eta-2) \\ N_3 &= \frac{1}{64}\xi\eta(\eta-2)(\xi+2) ; & N_4 &= \frac{1}{32}\xi(4-\eta^2)(\xi+2) \\ N_5 &= \frac{1}{64}\xi\eta(\eta+2)(\xi+2) ; & N_6 &= \frac{1}{32}\eta(4-\xi^2)(\eta+2) \\ N_7 &= \frac{1}{64}\xi\eta(\eta+2)(\xi-2) ; & N_8 &= \frac{1}{32}\xi(4-\eta^2)(\xi-2) \\ N_9 &= \frac{1}{16}(4-\eta^2)(4-\xi^2) & \text{and} \\ M_1 &= \frac{1}{4}(1-\xi)(1-\eta) ; & M_2 &= \frac{1}{4}(1+\xi)(1-\eta) \\ M_3 &= \frac{1}{4}(1+\xi)(1+\eta) ; & M_4 &= \frac{1}{4}(1-\xi)(1+\eta) \end{aligned} \quad (3.4)$$

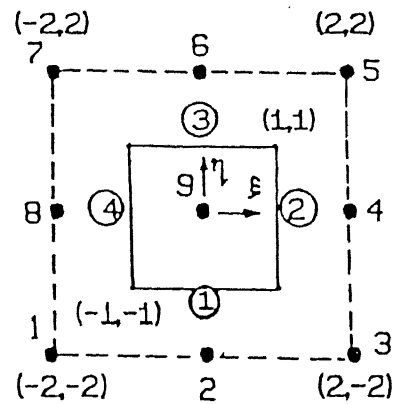
The integrals appearing in equations (2.13)-(2.16) have been evaluated using Gauss-Legendre quadrature. This is done by mapping the non-orthogonal control volume into a square computational cell whose co-ordinates vary from -1 to 1 in both the directions (Fig.4). The mapping is done by isoparametric transformation.

1, 2 ... 9 - Node numbers

①, ② - ④ - Side numbers



Physical domain
CV2



Computational domain

Fig.4 Transformation of a curvilinear control volume into a square computational cell.

The co-ordinates x and y for any point within the non-orthogonal control volume are interpolated in terms of their nodal values in much the same way as the flow variables. The interpolation scheme for the control volume CV2 are given by

$$X = \sum_{k=1}^9 N_k X_k ; Y = \sum_{k=1}^9 N_k Y_k \quad (3.5)$$

where (X_k, Y_k) are the co-ordinates of the nodes surrounding the control volume as shown in Fig 3(b). For continuity cells (CV1), the linear transformation is used in the form

$$X = \sum_{k=1}^4 M_k X_k ; Y = \sum_{k=1}^4 M_k Y_k \quad (3.6)$$

With the above transformation the integrals appearing in the equations (2.13)-(2.16) can be rewritten in the form of transformed co-ordinates ξ and η . For all the mapped cells, ξ and η vary from -1 to 1, and the Gauss-Legendre quadrature can be easily adopted for evaluating the integrals. The area integral is given by

$$\int_{-1}^1 \int_{-1}^1 F(\xi, \eta) d\xi d\eta = \sum_{k=1}^m \sum_{l=1}^m F(\xi_k, \eta_l) w_k w_l \quad (3.7)$$

where (ξ_k, η_l) are the Gauss points and w_k , and w_l are the corresponding weights. The co-ordinates of the Gauss sampling points are the zeroes of the

m^{th} degree Legendre polynomials, where m is the total number of Gauss points used in a particular direction. In the present case it is chosen to be equal to

2. The line integral can be evaluated as

$$\int_{-1}^1 F(\xi) d\xi = \sum_{k=1}^m F(\xi_k) w_k$$

$$\int_{-1}^1 F(\eta) d\eta = \sum_{k=1}^m F(\eta_k) w_k$$

For the completion of the transformation, it is necessary to convert the arc lengths, areas, surface integrals, derivatives and integrals in the physical coordinate system to the computational co-ordinates ξ and η . For the typical control volume **CV2** (Fig. 4) chain rule may be applied in the following

$$X = X(\xi, \eta) ; Y = Y(\xi, \eta)$$

$$dX = \frac{\partial X}{\partial \xi} d\xi + \frac{\partial X}{\partial \eta} d\eta ; dY = \frac{\partial Y}{\partial \xi} d\xi + \frac{\partial Y}{\partial \eta} d\eta$$

or in the matrix form

$$\begin{bmatrix} dX \\ dY \end{bmatrix} = \begin{bmatrix} \frac{\partial X}{\partial \xi} & \frac{\partial X}{\partial \eta} \\ \frac{\partial Y}{\partial \xi} & \frac{\partial Y}{\partial \eta} \end{bmatrix} \begin{bmatrix} \partial \xi \\ \partial \eta \end{bmatrix} = \begin{bmatrix} \sum_{k=1}^9 \frac{\partial N_k}{\partial \xi} X_k & \sum_{k=1}^9 \frac{\partial N_k}{\partial \eta} X_k \\ \sum_{k=1}^9 \frac{\partial N_k}{\partial \xi} Y_k & \sum_{k=1}^9 \frac{\partial N_k}{\partial \eta} Y_k \end{bmatrix} \begin{bmatrix} \partial \xi \\ \partial \eta \end{bmatrix}$$

in a similar fashion, the derivatives can be obtained as

$$\begin{bmatrix} \frac{\partial}{\partial \xi} \\ \frac{\partial}{\partial \eta} \end{bmatrix} = \begin{bmatrix} \frac{\partial X}{\partial \xi} & \frac{\partial Y}{\partial \xi} \\ \frac{\partial X}{\partial \eta} & \frac{\partial Y}{\partial \eta} \end{bmatrix} \begin{bmatrix} \frac{\partial}{\partial X} \\ \frac{\partial}{\partial Y} \end{bmatrix} = [J] \begin{bmatrix} \frac{\partial}{\partial X} \\ \frac{\partial}{\partial Y} \end{bmatrix} \quad (3.8)$$

where $[J]$ is the Jacobian matrix for the transformation. The matrix in the above equation can be evaluated using equations (3.4) and (3.5) in the definitions given above. From the equation (3.8), the velocity derivatives can be written as

$$\begin{bmatrix} \frac{\partial U}{\partial X} \\ \frac{\partial U}{\partial Y} \end{bmatrix} = [J]^{-1} \begin{bmatrix} \frac{\partial U}{\partial \xi} \\ \frac{\partial U}{\partial \eta} \end{bmatrix} = [J]^{-1} \begin{bmatrix} \frac{\partial N_1}{\partial \xi} & \frac{\partial N_2}{\partial \xi} & \frac{\partial N_3}{\partial \xi} \\ \frac{\partial N_1}{\partial \eta} & \frac{\partial N_2}{\partial \eta} & \frac{\partial N_3}{\partial \eta} \end{bmatrix} \begin{bmatrix} U_1 \\ U_2 \\ \vdots \\ U_9 \end{bmatrix} \quad (3.9)$$

Similarly we can evaluate the derivatives of V, θ .

On the s th side ($s=1,2,3,4$) the elemental length vector dl_s is

$$\begin{aligned} dl_s &= dX_s \hat{i} + dY_s \hat{j} \\ &= \left\{ \left(\frac{\partial X}{\partial \xi} \right)_s d\xi + \left(\frac{\partial X}{\partial \eta} \right)_s d\eta \right\} \hat{i} \\ &\quad + \left\{ \left(\frac{\partial Y}{\partial \xi} \right)_s d\xi + \left(\frac{\partial Y}{\partial \eta} \right)_s d\eta \right\} \hat{j} \end{aligned} \quad (3.10)$$

The outward unit normal vectors on the corresponding cell boundaries are given by

$$\hat{n}_s = \left\{ \frac{\left(\frac{\partial Y}{\partial \zeta} \right)_s \hat{i} - \left(\frac{\partial X}{\partial \zeta} \right)_s \hat{j}}{\left(\frac{\partial l}{\partial \zeta} \right)_s} \right\} (-1)^m \quad (3.11)$$

where $m = 0$ for $s=1,2$ and $m=1$ for $s=3,4$ and

$$\left(\frac{dl}{d\zeta} \right)_s = \sqrt{\left(\frac{\partial X}{\partial \zeta} \right)_s^2 + \left(\frac{\partial Y}{\partial \zeta} \right)_s^2} \quad (3.12)$$

$\zeta = \xi$ for $s=1,3$ and $\zeta = \eta$ for $s=2,4$. The elemental length, dl is represented as

$$dl = \left(\frac{\partial l}{\partial \xi} \right)_s d\xi \quad (3.13)$$

for the sides 1 and 3, since η is constant for these sides. Similarly

$$dl = \left(\frac{\partial l}{\partial \eta} \right)_s d\eta \quad (3.14)$$

for sides 2 and 4, since ξ is constant for these sides.

Lastly , the elemental area dA can be evaluated as

$$dA = |J| d\xi d\eta \quad (3.15)$$

For continuity control volume, it is not necessary to employ the numerical quadrature, since the shape of CV1 is simpler and the velocity interpolation

is linear.

Using the interpolation as described above the final form of momentum and energy equations can be written in the matrix form as

$$\begin{Bmatrix} \dot{U} \\ \dot{V} \\ \dot{\theta} \end{Bmatrix} = [[C] + [D]] \begin{Bmatrix} U \\ V \\ \theta \end{Bmatrix} + [S] [P] + [Sr] \quad (3.16)$$

where

$$[C] = \begin{bmatrix} C_{1j} & 0 & 0 \\ 0 & C_{2j} & 0 \\ 0 & 0 & C_{3j} \end{bmatrix} \quad (3.17)$$

and the elements C_{1j} , C_{2j} and C_{3j} are given by

$$[C_{1j}] = [C_{2j}] = [C_{3j}] = \frac{-1}{A_{cv2}} \int_{cs2} N_j (U n_x + V n_y) dl = \frac{-1}{A_{cv2}} \sum_{s=1}^4 \sum_{k=1}^2 \left[N_j \sum_{q=1}^9 (U_q n_x + V_q n_y) N_q \right] w_k \Delta l_s \quad (3.18)$$

The matrix $[D]$ in equation (3.16) is given by

$$[D] = \begin{bmatrix} DU_{1j} & DV_{1j} & 0 \\ DU_{2j} & DV_{2j} & 0 \\ 0 & 0 & D\theta_{3j} \end{bmatrix} \quad (3.19)$$

where

$$\begin{aligned}
DU_{1j} &= \frac{1}{A_{cv2}} \int_{cs2} \left(\frac{2}{Re} \frac{\partial N_j}{\partial X} n_x + \frac{1}{Re} \frac{\partial N_j}{\partial Y} n_y \right) dl \\
&= \frac{1}{A_{cv2}} \sum_{s=1}^4 \sum_{k=1}^2 \left[\frac{2}{Re} \frac{\partial N_j}{\partial X} n_x + \frac{1}{Re} \frac{\partial N_j}{\partial Y} n_y \right] w_k \Delta l_s
\end{aligned} \quad (3.20)$$

$$\begin{aligned}
DU_{2j} &= \frac{1}{A_{cv2}} \int_{cs2} \left(\frac{1}{Re} \frac{\partial N_j}{\partial Y} n_x \right) dl \\
&= \frac{1}{A_{cv2}} \sum_{s=1}^4 \sum_{k=1}^2 \left[\frac{1}{Re} \frac{\partial N_j}{\partial Y} n_x \right] w_k \Delta l_s
\end{aligned} \quad (3.21)$$

$$\begin{aligned}
DV_{1j} &= \frac{1}{A_{cv2}} \int_{cs2} \left(\frac{1}{Re} \frac{\partial N_j}{\partial X} n_y \right) dl \\
&= \frac{1}{A_{cv2}} \sum_{s=1}^4 \sum_{k=1}^2 \left[\frac{1}{Re} \frac{\partial N_j}{\partial X} n_y \right] w_k \Delta l_s
\end{aligned} \quad (3.22)$$

$$\begin{aligned}
DV_{2j} &= \frac{1}{A_{cv2}} \int_{cs2} \left(\frac{1}{Re} \frac{\partial N_j}{\partial X} n_x + \frac{2}{Re} \frac{\partial N_j}{\partial Y} n_y \right) dl \\
&= \frac{1}{A_{cv2}} \sum_{s=1}^4 \sum_{k=1}^2 \left[\frac{1}{Re} \frac{\partial N_j}{\partial X} n_x + \frac{2}{Re} \frac{\partial N_j}{\partial Y} n_y \right] w_k \Delta l_s
\end{aligned} \quad (3.23)$$

$$\begin{aligned}
D\theta_{3j} &= \frac{1}{A_{cv2}} \int_{cs2} \frac{1}{Pr Re} \left(\frac{\partial N_j}{\partial X} n_x + \frac{\partial N_j}{\partial Y} n_y \right) dl \\
&= \frac{1}{A_{cv2}} \sum_{s=1}^4 \sum_{k=1}^2 \frac{1}{Pr Re} \left[\frac{\partial N_j}{\partial X} n_x + \frac{\partial N_j}{\partial Y} n_y \right] w_k \Delta l_s
\end{aligned} \quad (3.24)$$

The pressure matrix in turn is

$$[\mathbf{S}] = \begin{bmatrix} \mathbf{S}_{1j} \\ \mathbf{S}_{2j} \\ \mathbf{0} \end{bmatrix} \quad (3.25)$$

where

$$\mathbf{S}_{1j} = -\frac{1}{A_{cv2}} \int M_j n_x dl = -\frac{1}{A_{cv2}} \sum_{s=1}^4 \sum_{k=1}^2 (M_j n_x) w_k \Delta l_s \quad (3.26)$$

$$\mathbf{S}_{2j} = -\frac{1}{A_{cv2}} \int M_j n_y dl = -\frac{1}{A_{cv2}} \sum_{s=1}^4 \sum_{k=1}^2 (M_j n_y) w_k \Delta l_s \quad (3.27)$$

Lastly, the buoyancy term $[Sr]$ can be expressed as

$$[Sr] = \begin{bmatrix} 0 \\ Sr_2 \\ 0 \end{bmatrix} \quad (3.28)$$

where

$$Sr_2 = \frac{1}{A_{cv2}} \frac{Gr}{Re^2} \int \int_{cv2} \theta dA = \frac{Gr}{Re^2} \theta_{av} \quad (3.29)$$

where θ_{av} is the non-dimensional temperature at the center of the control volume **CV2**.

The continuity equation can be discretised as

$$\sum_{s=1}^4 (\bar{U}_s n_{x,s} + \bar{V}_s n_{y,s}) \Delta l_s = 0 \quad (3.30)$$

3.2 Upwinding of Convection Terms

In the numerical solution of Navier-Stokes equation, the convection terms need specific attention for conserving the transportive property. An effective upwind discretisation for the convection terms is implemented by setting

$$C_{1j} U_j = C_{2j} U_j = \frac{1}{A_{cv2}} \int (U n_x + V n_y) G_j U_j dl \quad (3.31)$$

where G_j is the upwind basis function, and is given by

CENTRAL LIBRARY
I.I.T. KANPUR
No. A 125482

$$\sum_{j=1}^9 G_j U_j = \sum_{j=1}^9 (1 - \alpha) N_j U_j + \alpha U_b \quad (3.32)$$

The subscript b corresponds to the node situated upstream of the concerned face and α is the upwinding factor. For purely symmetric interpolation $\alpha = 0$ and for the upwind biased interpolation, $\alpha = 1$. In all my computations, I have used $\alpha=0$ so that there is no artificial viscosity.

3.3 Derivation of Pressure Correction Equation

When the time gradient of velocities and temperature are expressed in the discretized form, equation (20) becomes

$$\begin{Bmatrix} U^{n+1} \\ V^{n+1} \end{Bmatrix} = \begin{Bmatrix} U^n \\ V^n \end{Bmatrix} + \Delta\tau [\mathbf{C}^n + \mathbf{D}^n] \begin{Bmatrix} U^n \\ V^n \end{Bmatrix} + \Delta\tau [\mathbf{S}] \{P^{n+1}\} + [\mathbf{Sr}]^n \quad (3.33)$$

where the subscripts n and $n + 1$ denote time levels. However, at the start of calculation for each time step, P^{n+1} is not known and hence equation (3.33) predicts provisional velocities (represented by a superscript asterisk *) that satisfy momentum balance corresponding to the p^n pressures. When both pressure and velocities undergo iterative corrections, P^n takes up provisional value P^* . Thus

$$\begin{Bmatrix} U^* \\ V^* \end{Bmatrix} = \begin{Bmatrix} U^n \\ V^n \end{Bmatrix} + \Delta\tau [\mathbf{C}^n + \mathbf{D}^n] \begin{Bmatrix} U^n \\ V^n \end{Bmatrix} + \Delta\tau [\mathbf{S}] \{P^*\} + [\mathbf{S}]^n \quad (3.34)$$

As the continuity equation is satisfied in each cell, all provisional velocities reach the final values for the time step ($n+1$). Subtracting equation (3.34) from equation (3.33) the expressions for the velocity corrections can be obtained as

$$\left\{ \begin{array}{l} U^{n+1} - U^* \\ V^{n+1} - V^* \end{array} \right\} = \left\{ \begin{array}{l} \delta U \\ \delta V \end{array} \right\} = \Delta\tau [S] \delta P \quad (3.35)$$

where δU , δV and δP are the velocity and pressure corrections, respectively.

Applying the principle of continuity at the $(n+1)$ th level,

$$\sum_{s=1}^4 (\bar{U}_s^{n+1} n_{xs} + \bar{V}_s^{n+1} n_{ys}) \Delta l_s = 0 \quad (3.36)$$

The uncorrected velocities, however, do not satisfy the continuity equation, leading to a non-zero residue of the form

$$\sum_{s=1}^4 (\bar{U}_s^* n_{xs} + \bar{V}_s^* n_{ys}) \Delta l_s = R \quad (3.37)$$

Subtracting equation (3.36) from equation (3.37), we obtain

$$\sum_{s=1}^4 (\delta \bar{U}_s n_{xs} + \delta \bar{V}_s n_{ys}) \Delta l_s = -R \quad (3.38)$$

where $\delta \bar{U}_s$ and $\delta \bar{V}_s$ are the average corrections on the s th side, so as to satisfy mass continuity in the control volume. The quantities $\delta \bar{U}_s$ and $\delta \bar{V}_s$ are expressed in terms of the nodal velocity corrections, which in turn are substituted by proper pressure corrections using equation (3.35). These average

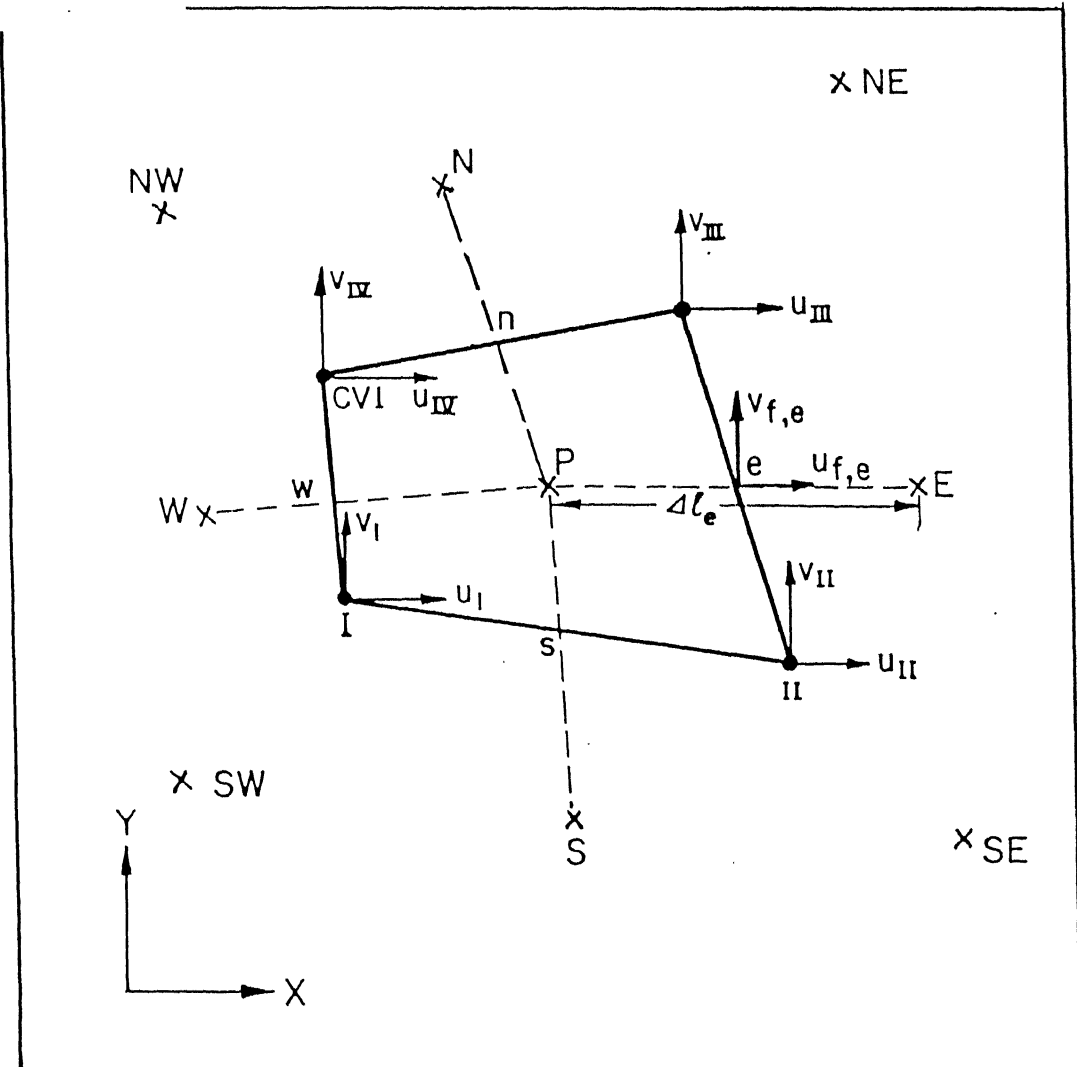


Fig.5 Pressure-velocity coupling for a continuity control volume.

velocity corrections, when evaluated as the simple average of the nodal velocities, lead to decoupling of pressure in alternate continuity cells. This decoupling of pressure variable was also observed by Majumdar *et al* [17].

Introducing face-center velocity corrections $U_{f,s}$, $V_{f,s}$ as shown in Fig.5, the average corrections on the east side of the CV1 can be expressed as

$$\delta\overline{U_e} = \frac{1}{6}\delta U_{II} + \frac{1}{6}\delta U_{III} + \frac{4}{6}\delta U_{f,e} \quad (3.39)$$

$$\delta\overline{V_e} = \frac{1}{6}\delta V_{II} + \frac{1}{6}\delta V_{III} + \frac{4}{6}\delta V_{f,e} \quad (3.40)$$

where II and III are the velocity nodes lying on the east face. Similarly, the average corrections on the other sides can also be estimated. Note that equations (3.39) and (3.40) amounts to the application of Simpson's rule along the boundaries of CV1. In order to find the expression for $\delta U_{f,e}$, $\delta V_{f,e}$ a modified form of the equation (3.35) can be written for the velocity correction vector as

$$\delta V = -\delta\tau\Delta(\delta P) \quad (3.41)$$

eventually we can write

$$\begin{aligned} \delta U_{f,e} &= (\hat{i} \cdot \delta V)_{f,e} = -\delta\tau \hat{i} \cdot \left\{ \hat{c} \frac{\delta P_E - \delta P_P}{\Delta l_E} \right\} \\ &= \Delta\tau \left\{ \frac{X_E - X_P}{\Delta l_E} \right\} \left\{ \frac{\delta P_E - \delta P_P}{\Delta l_E} \right\} \end{aligned} \quad (3.42)$$

Similarly,

$$\delta V_{f,e} = \Delta\tau \left\{ \frac{Y_E - Y_P}{\Delta l_E} \right\} \left\{ \frac{\delta P_E - \delta P_P}{\Delta l_E} \right\} \quad (3.43)$$

Here \hat{e} is the unit vector connecting the central pressure node P to the eastern neighbouring pressure node E. Similarly, the face-center velocity corrections can be obtained as

$$\begin{aligned} \delta U_{f,(n,w,s)} &= \Delta\tau \left\{ \frac{X_{(N,W,S)} - X_P}{\Delta l_{(N,W,S)}} \right\} \left\{ \frac{\delta P_P - \delta P_{(N,W,S)}}{\Delta l_{(N,W,S)}} \right\} \\ \delta V_{f,(n,w,s)} &= \Delta\tau \left\{ \frac{Y_{(N,W,S)} - Y_P}{\Delta l_{(N,W,S)}} \right\} \left\{ \frac{\delta P_P - \delta P_{(N,W,S)}}{\Delta l_{(N,W,S)}} \right\} \end{aligned} \quad (3.44)$$

where the lower-case subscripts (n, w, s) refer to the corresponding boundary faces, while the upper-case subscripts (N, W, S) refer to the corresponding continuity cells. The mass residue contribution R_e to the east face is given by

$$\Delta l_e (\delta \bar{U}_e n_{x,e} + \delta \bar{V}_e n_{y,e}) = -R_e \quad (3.45)$$

Substituting for δU_e and δV_e from equations (3.39) and (3.40), we have

$$\Delta l_e \left\{ \frac{1}{6} \delta U_{II} + \frac{1}{6} \delta U_{III} + \frac{4}{6} \delta U_{f,e} \right\} n_{x,e} + \Delta l_e \left\{ \frac{1}{6} \delta V_{II} + \frac{1}{6} \delta V_{III} + \frac{4}{6} \delta V_{f,e} \right\} n_{y,e} = -R_e \quad (3.46)$$

From equation (3.35), the nodal velocity corrections are given by

$$\begin{Bmatrix} \delta U_{II} \\ \delta V_{II} \end{Bmatrix} = \Delta \tau [S]_{II} \{ \delta p_S \quad \delta p_{SE} \quad \delta p_E \quad \delta p_P \ }^T \quad (3.47)$$

$$\begin{Bmatrix} \delta U_{III} \\ \delta V_{III} \end{Bmatrix} = \Delta \tau [S]_{III} \{ \delta p_N \quad \delta p_{NE} \quad \delta p_E \quad \delta p_P \ }^T \quad (3.48)$$

It is to be noted that in equations (3.47) and (3.48) the pressure coefficient matrix S is evaluated at the nodes. After substituting equations (3.42),(3.43),(3.47) and (3.48) into equation (3.46), the residue contribution of the east face, R_e , can be calculated in terms of pressure corrections. Similar exercise for the other sides of the continuity cells would lead to a pressure correction equation of the form

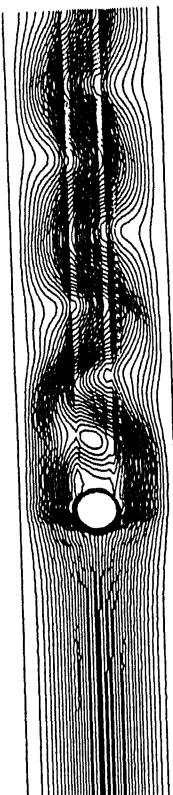
$$[\mathbf{CP}] \{ \delta P \} = -R \quad (3.49)$$

where \mathbf{CP} is the coefficient matrix corresponding to the pressure correction array and R is the mass residue arising from velocities updated by momentum equations.

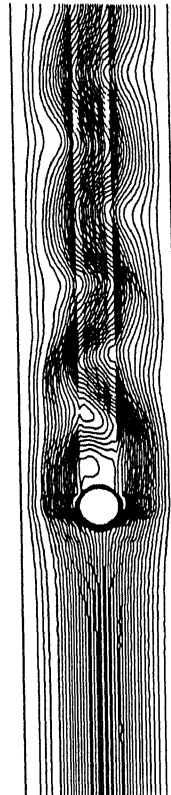
Chapter 4

RESULTS AND DISCUSSION

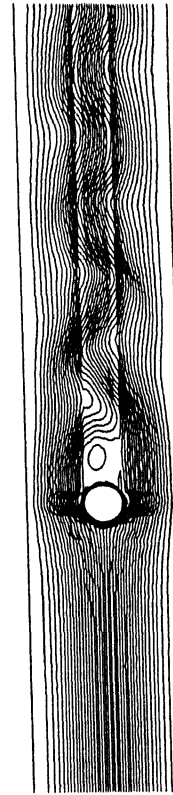
Air ($\text{Pr}=0.7$) has been used as the working fluid. Boussinesq approximation has been applied while writing the momentum equations. The results are obtained for a Reynolds number of 100 and for different values of Richardson number. Streamlines for various Richardson numbers have been plotted in Fig. 6. These plots correspond to a dynamic steady state behaviour. The physical significance of negative Richardson number is culmination of a buoyancy force in a direction opposite to the flow direction. In the viscous region, at the vicinity of the aft of the cylinder, the inertia force is opposed by the force due to adverse pressure gradient, the negative buoyancy force and the viscous force. Depending on the magnitude of Richardson number, the point of separation moves towards the leading edge causing an early separation. This also broadens the wake. Vortex shedding becomes quite prominent in the entire regime of negative Richardson number. The shedding phenomenon continues



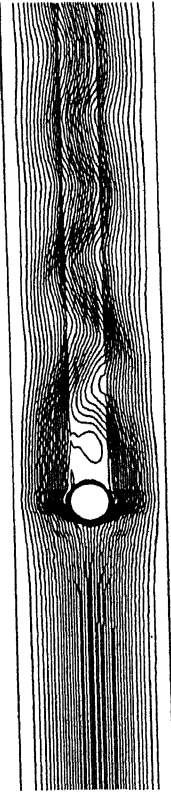
$Ri = -1.0$



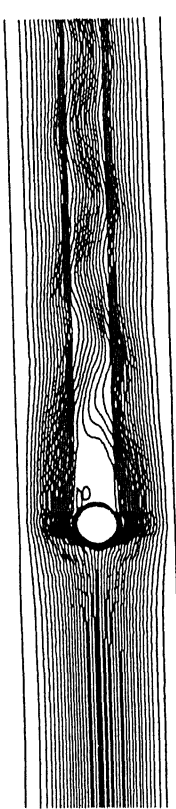
$Ri = -0.5$



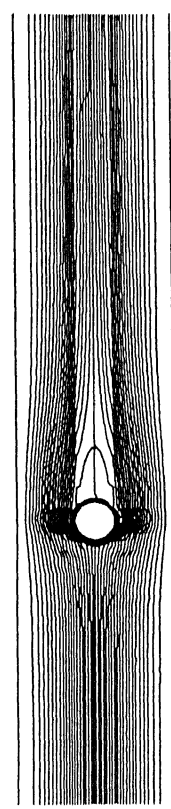
$Ri = -0.1$



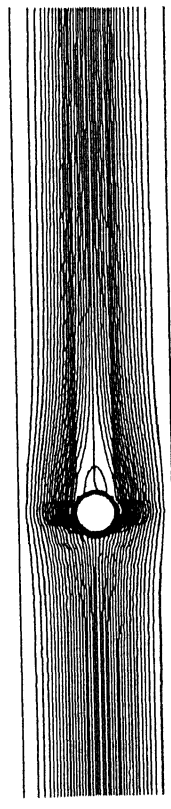
$Ri = 0$



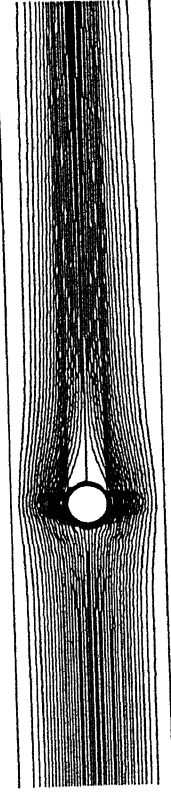
$Ri = 0.1$



$Ri = 0.2$

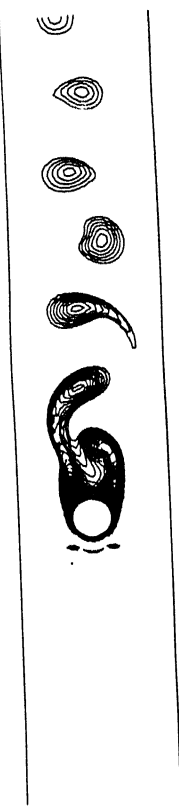


$Ri = 0.5$

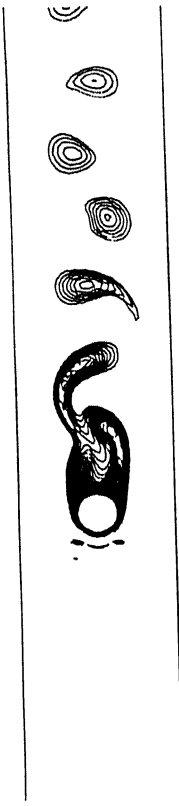


$Ri = 1.0$

Fig.6 Streamlines



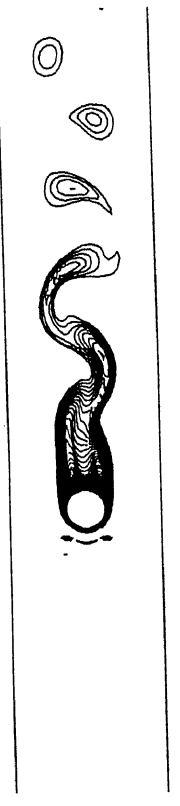
$Ri = -1.0$



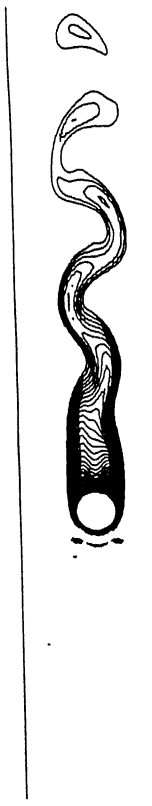
$Ri = -0.5$



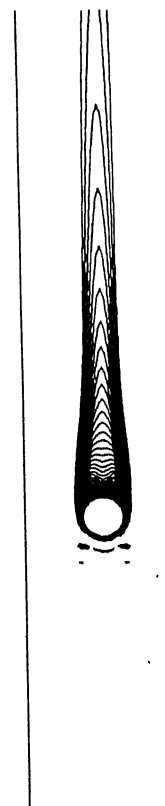
$Ri = -0.1$



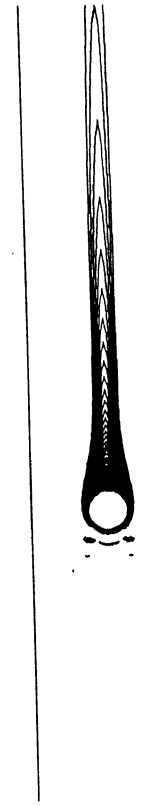
$Ri = 0$



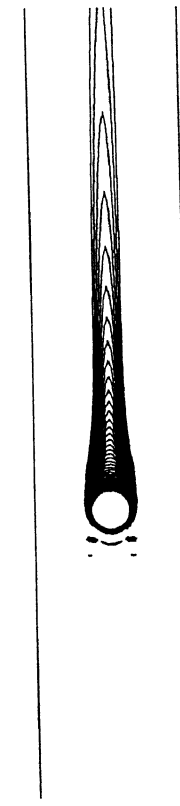
$Ri = 0.1$



$Ri = 0.2$

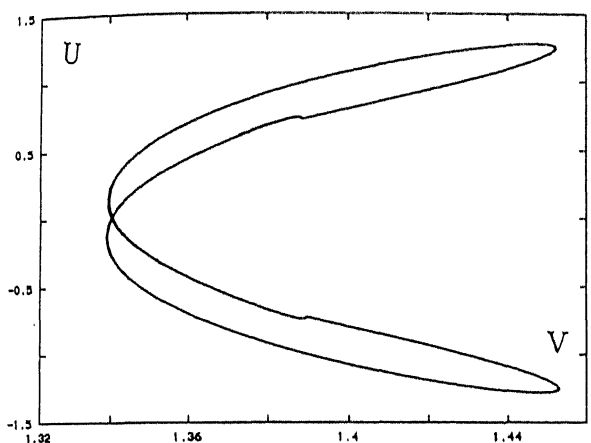


$Ri = 0.5$

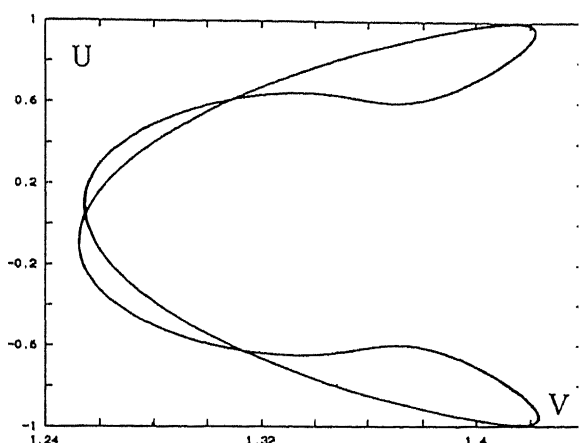


$Ri = 1.0$

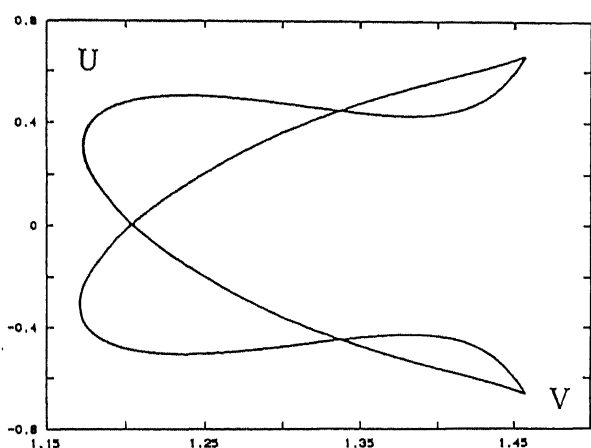
to characterize the flow even at $Ri=0$ and $Ri=0.1$. For a Richardson number of 0.15(not shown here) and above, the flow structure becomes different. The aiding buoyancy changes the dynamics altogether. Near the vicinity of the cylinder, even at the aft, the buoyancy force is added up with the inertia force in the face of pressure force and viscous force. This results in a separation delay and the vortex shedding is also stopped. This observation is in confirmation with the earlier studies by Noto and Matsumoto [10, 11, 12] and Chang and Sa [13]. Figure 7 shows isotherms for various Richardson numbers. The buoyancy opposed and buoyancy aiding cases are discerned in this figure. It can readily be appreciated that the waviness of the isotherms in the downstream of the cylinder is more for the buoyancy opposed convection as compared to buoyancy aiding convection. Beyond a Richardson number of 0.2 the plume spread becomes narrow and waviness disappears. Figure 8 shows the phase diagram for different Richardson numbers. For all the Richardson numbers, the transverse velocity component at a point 3D downstream of the cylinder has been plotted against the streamwise velocity component at the same point. These plots clearly establish the periodic nature of the flow for all the cases below a Richardson number of 0.15. The orbits of the phase-diagram also indicate superimposition of oscillations with two different frequencies. The signal traces of the transverse velocity components and their FFT for the Richardson numbers of -1.0 and 0 have been shown in Fig 9. For the case



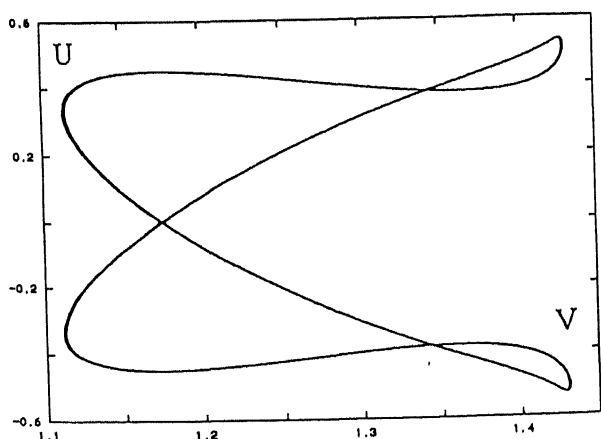
$Ri = -1.0$



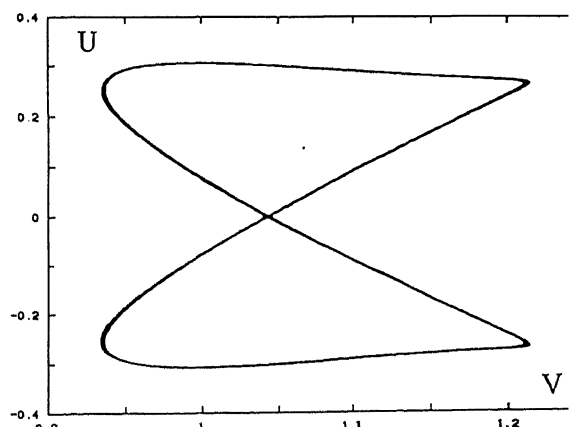
$Ri = -0.5$



$Ri = -0.1$

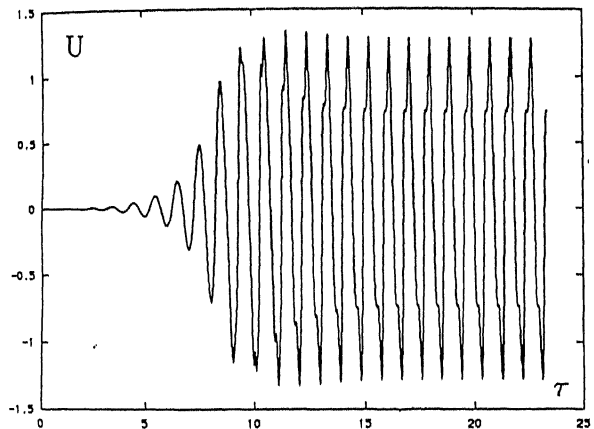


$Ri = 0$

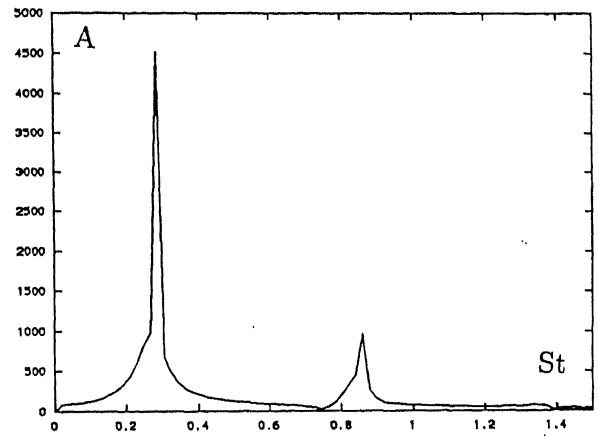


$Ri = 0.1$

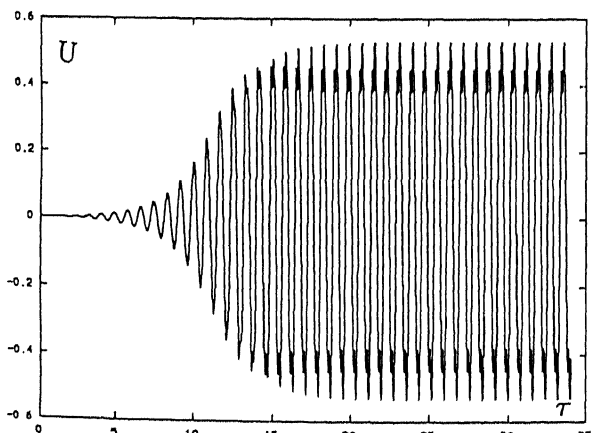
Fig.8 Phase diagrams (U vs. V plots)



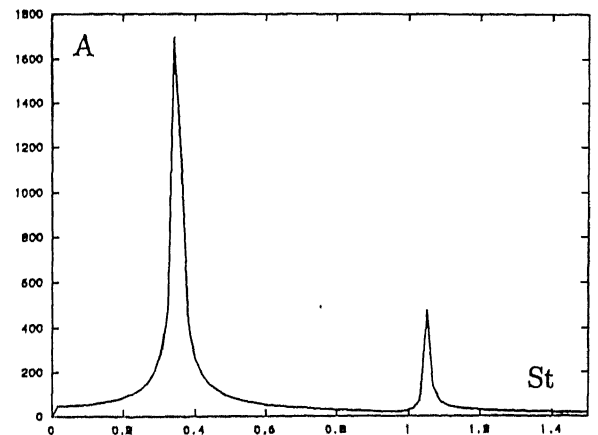
$Ri = -1.0$



$Ri = -1.0$



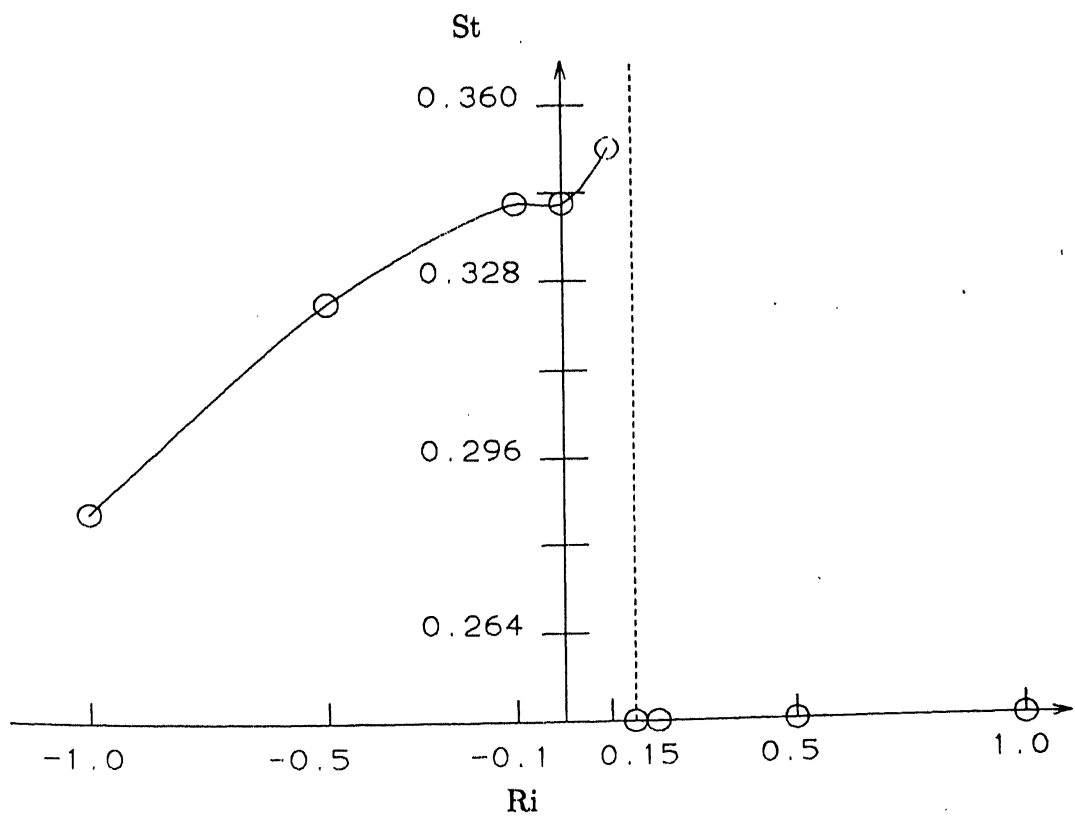
$Ri = 0$



$Ri = 0$

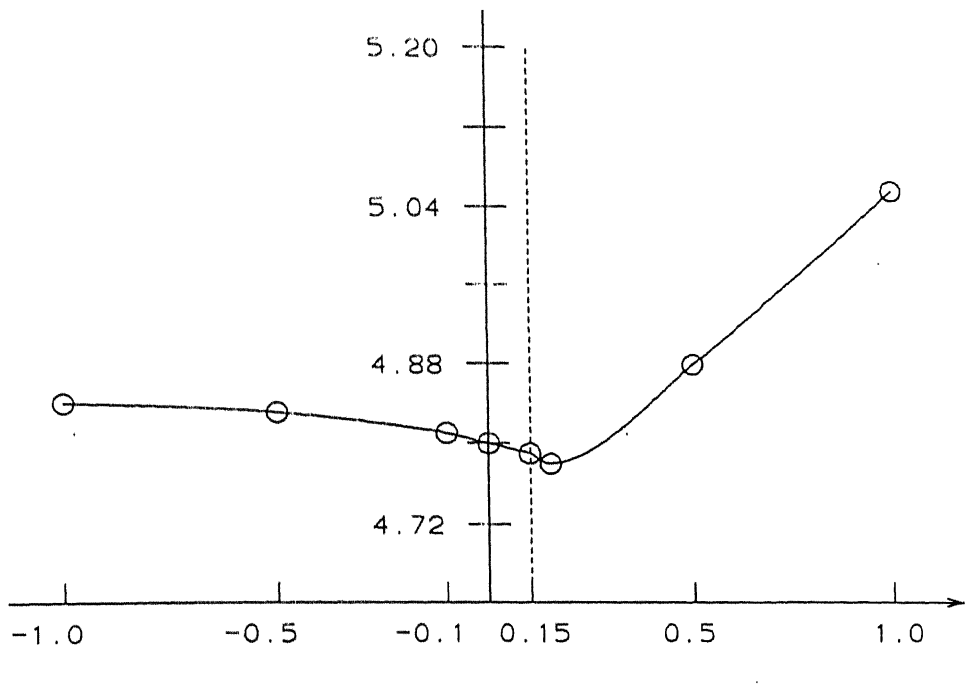
Fig.9 Transverse velocity signal vs. Non-dimensional time
and FFT for $Ri=-1.0$ and $Ri=0$ cases

of $Ri = -1.0$, the peaks at $St = 0.2861$ and $St = 0.8583$ confirms the presence of multiple frequencies (super harmonics). In the case of $Ri = 0$, we observe a similar trend which can be depicted as two component time series. Figure 10 shows the variation of Strouhal number for different Richardson numbers. At the first place, the shedding frequency is observed to decrease with increased cooling of the cylinder below the fluid temperature. The fluid in the wake becomes denser due to cooling and therefore the vortices stay attached to the cylinder for long. The broadening of the wake also helps in accommodating large size vortices which are shed in the downstream at greater time intervals. For Richardson number upto 0.1 the shedding frequency steadily increases but for $Ri \geq 0.15$ the shedding frequency suddenly becomes zero i.e, the shedding is stopped.



The temporal mean of the Nusselt number averaged over the entire cylinder surface has been plotted against the Richardson number in Fig.11. The behaviour of the average Nusselt number characteristic can also be explained on the basis of the above arguments. Over the range of positive Richardson number, increasing magnitude of Ri tends to increase the average Nusselt number but for negative Ri no significant change in Nusselt number is observed because of longer residence time of the large size vortices at the back of the cylinder. The reduced shedding frequency in the regime of negative Richardson number tends to reduce the heat transfer. However beyond the critical Ri of 0.15 the vortices becomes small in size and thus the zone of poor heat transfer is reduced. The increase in Nusselt number is totally attributed to the increase in the magnitude of Ri .

The time average value of the local Nusselt number Nu_ϕ has been plotted against the angle ϕ in Fig.12. The situation $\phi = 0$ corresponds to the stagnation point facing the incoming fluid. The angle increases downstream till the tail of the cylinder is reached. The initial increase in local Nusselt number (upto $\phi \approx 50^\circ$) is due to the increase in velocity of the fluid. As the fluid moves downstream from $\phi = 0$ the flow area reduces and therefore the velocity rises. The Nu_ϕ decreases with further increase in ϕ due to the growth of boundary layer on the cylinder. The minimum point is the point of separation. It can be readily observed that the separation point is delayed with heating of the



Ri

Fig.11 Average Nusselt number vs. Richardson number

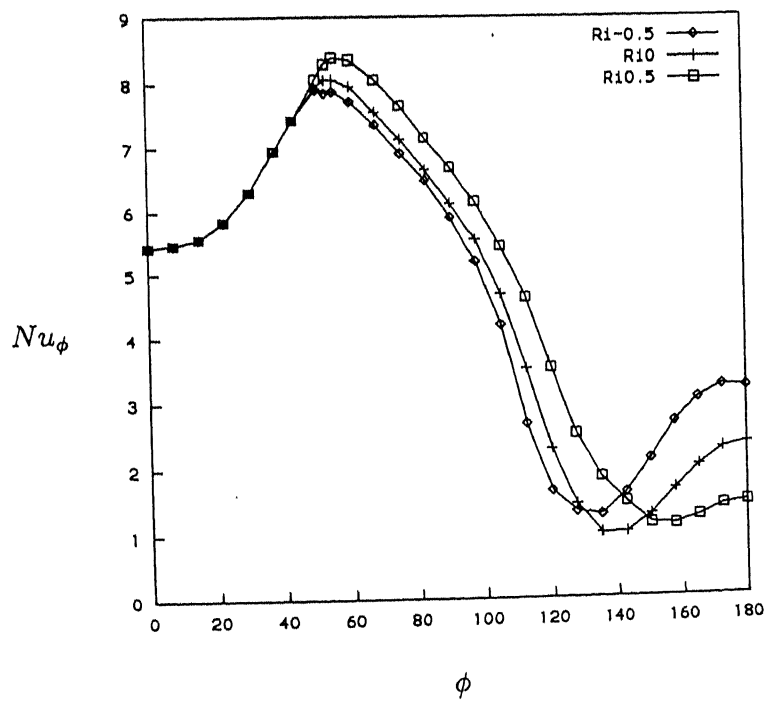
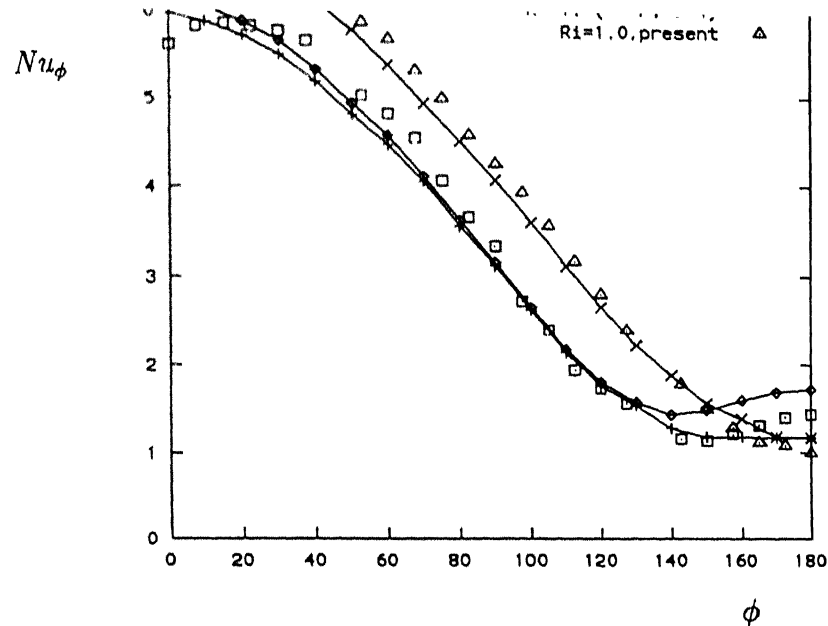


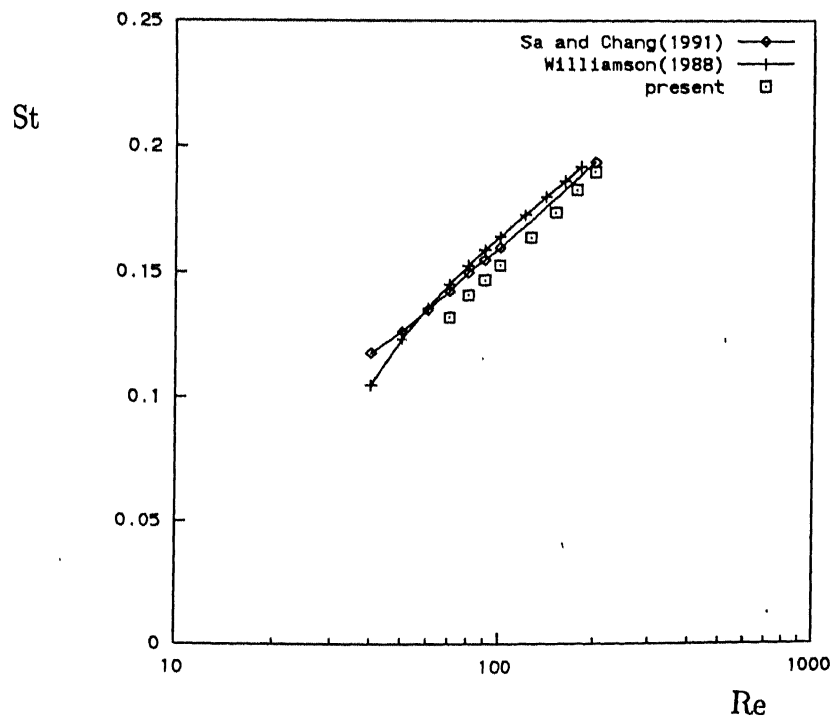
Fig.12 Local Nusselt number variation over the cylinder surface

cylinder. For negative Ri the heat transfer increases rapidly after the point of separation but for positive Ri there is no significant rise in local heat transfer. In case of heating of the cylinder the buoyancy aids the forced convection and therefore the back-flow is greatly reduced. This reduces the mass of fluid present near the cylinder after the point of separation. There is therefore no significant increase in heat transfer. In case of cooling of the cylinder, due to the buoyancy the fluid returns back after separation and is responsible for the rapid increase in heat transfer after the point of separation for negative Ri case.

For comparison with earlier studies, the channel width has been enhanced. The blockage ratiood (D/H) of 0.1 and the far field boundary condition for the confining walls have been deployed. The Reynolds number of interest is 40 and the Richardson numbers are zero and unity. The comparisons of local Nusselt number distribution has been shown in Fig.13(a). The results are in good agreement with the local Nusselt number distribution obtained by Badr [7] and Dennis *et al* [19]. Variation of Strouhal numbers as a function of Reynolds number has been shown in Fig. 13(b). All the computations have simulated flow past a cylinder in an infinite medium. The Strouhal numbers obtained in the present computation agree well with those due to Williamson [20] and Sa and Chang [21].



(a) Local Nusselt number



(b) Strouhal number

Fig.13 Comparison of results

Chapter 5

CONCLUSION

A novel finite volume algorithm has been successfully extended to simulate a complex mixed convection flow in a vertical channel with a built-in circular cylinder.

Two different flow regimes, depending on whether Richardson number is less than or greater than a critical value of 0.15 have been identified. The regime with $Ri < 0.15$ is characterized by broadening of the wake, advanced flow separation and strong vortex shedding. The other regime ($Ri > 0.15$) represents increased separation delay and a zone of twin vortices attached to the cylinder. The Strouhal number reduces as the cylinder is cooled below the fluid temperature. Formation of large size vortices and reduced shedding frequency do not enhance heat transfer significantly for larger value of negative Richardson number. For $Ri > 0.15$ no vortex shedding takes place and the wake is also reduced in size. In this regime there is significant increase in average Nusselt number with increase in the magnitude of Richardson number.

Bibliography

- [1] Fromm J. E. and Harlow F. H. (1963), Numerical Solution of the Problem of Vortex Street Development, *Phys. Fluids*, vol. 6, 975
- [2] Thoman D. C. and Szewczyk A. A. (1969), Time Dependent Viscous Flow over Circular Cylinder, *Phys. Fluids*, vol. 12, 1176
- [3] Jain P. C. and Goel B. S. (1976), A Numerical study of Unsteady Laminar Forced Convection from a Circular Cylinder, *J. Heat Transfer*, vol. 98, 303
- [4] Kundu D., Haji-Sheikh and Lou Y.S.(1991), Pressure and heat transfer in cross flow over cylinders between two parallel plates, *Numerical Heat Transfer, Part A*, vol. 19, 345
- [5] Kundu D., Haji-Sheikh and Lou Y.S.(1991), Heat transfer predictions in cross flow over cylinders between two parallel plates, *Numerical Heat Transfer, Part A*, vol. 19, 361
- [6] Farouk B. and Guceri S. I. (1982), Natural and Mixed Convection Heat Transfer around a Horizontal Cylinder wihtin Confining Walls, *Numerical*

Heat Transfer, vol. 5, 329

- [7] Badr H. M. (1984), Laminar combined convection from a horizontal cylinder-parallel and contrafow regimes, *Int. J. Heat Mass Transfer*, vol. 27, 15
- [8] Biswas G., Laschenski H., Mitra N. K. and Fiebig M. (1990), Numerical Investigation of Mixed Convection Heat Transfer in a Horizontal Channel with a built-in Square Cylinder, *Numerical Heat Transfer, Part A*, vol. 18, 173
- [9] Oosthuizen P. H. and Madan S. (1971), The effect of flow direction on combined convective heat transfer from cylinders to air, *Trans. ASME C: J. Heat Transfer*, vol. 93, 240
- [10] Noto K. and Matsumoto R. (1985), A breakdown of the Karman vortex street due to the natural convection, *Flow Visualization III*, p.348, Springer
- [11] Noto K. and Matsumoto R. (1987a), Numerical simulation on development of the Karman vortex street due to the negative buoyant force, *Proc. Numerical Methods in Laminar and Turbulent Flow*, vol. 5, 796, Pineridge

- [12] Noto K. and Masumoto R. (1987b), Breakdown of the Karman vortex street due to natural convection (case from an elliptical cylinder whose major axis oriented at right angle to the main stream), *Proc. Numerical Methods in Thermal Problems*, vol. 5, 484, Pineridge
- [13] Chang K. S. and Sa J. Y. (1990), The effect of buoyancy on vortex shedding in the near wake of a circular cylinder, *J. Fluid Mech.*, vol. 220, 253
- [14] Mukhopadhyay A., Sundararajan T. and Biswas G. (1993), An explicit transient algorithm for predicting incompressible viscous flows in arbitrary geometry, *Int. J. for Numerical Methods in Fluids*, vol. 17, 975
- [15] Harlow F.H. and Welch J.E.(1965) Numerical calculation of Time-Dependent viscous incompressible flow of fluid with free surface,*Phys. Fluids*, vol.8, 2182
- [16] Patankar S.V. and Spalding D.B.(1972), A calculation procedure for heat,mass and momentum transfer in three dimensional parabolic flows,*Int. J. Heat Mass Tr.*, vol.15, 1787
- [17] Majumdar S., Rodi W. and Vanka S.P.(1987) On the use of non-staggered pressure-velocity arrangement for numerical solution of incompressible flows, *Int. J. Num. Methods Fluids*, vol.17, 975

- [18] Reddy J. N.(1993), An introduction to the finite element method, Second ed., Mc-Graw Hill
- [19] Dennis S. G. R. and Chang. G.(1970), Numerical solutions for steady flow past a circular cylinder at Reynolds numbers upto 100, *J. Fluid Mech.*, vol. 42, 471
- [20] Williamson C. H. K.(1988), Defining a universal and continuous Strouhal-Reynolds number relationship for the laminar vortex shedding of a circular cylinder, *Phys. Fluids*, vol. 31, 2742
- [21] Sa J.Y and Chang K.S.(1991), Shedding patterns of the near-wake vortices behind a circular cylinder, *Int. J. Num. Methods. Fluids*, vol. 12, 463